ELSEVIER

Contents lists available at ScienceDirect

Composites Part A

journal homepage: www.elsevier.com/locate/compositesa





Sub-microscale speckle pattern creation on single carbon fibers for scanning electron microscope-digital image correlation (SEM-DIC) experiments

Karan Shah ^{a,b}, Subramani Sockalingam ^{a,b,*}, Hannah O'Brien ^{a,b}, Gene Yang ^b, Mohammad EL Loubani ^b, Dongkyu Lee ^b, Michael A. Sutton ^b

ARTICLE INFO

Keywords: Fibers Microscale SEM-DIC

ABSTRACT

High performance carbon fibers are widely used as fiber reinforcements in composite material systems for aerospace, automotive, and defense applications. Longitudinal tensile failure of such composite systems is a result of clustering of single fiber tensile failures occurring at the microscale, on the order of a few microns to a few hundred microns. Since fiber tensile strength at the microscale has a first order effect on composite strength, it is important to characterize the strength of single fibers at microscale gage lengths which is extremely challenging. An experimental technique based on a combination of transverse loading of single fibers under SEM with DIC is a potential approach to access microscale gage lengths. The SEM-DIC technique requires creation of uniform, random, and contrastive sub-microscale speckle pattern on the curved fiber surface for accurate strain measurements. In this paper, we investigate the formation of such sub-microscale speckle patterns on individual sized IM7 carbon fibers of nominal diameter 5.2 µm via sputter coating. Various process conditions such as working pressure, sputtering current, and coating duration are investigated for pattern creation on fiber surface using a gold-palladium (Au-Pd) target. A nanocluster type sub-microscale pattern is obtained on the fiber surface for different coating conditions. Numerical translation experiments are performed using the obtained patterns to study image correlation and identify a suitable pattern for SEM-DIC experiments. The pattern obtained at a working pressure of 120-140 mTorr with 50 mA current for a duration of 10 min is found to have an average speckle size of 53 nm and good contrast for image correlation. Rigid body translation SEM experiments for drift/ distortion correction using a sized IM7 carbon fiber coated with the best patterning conditions showed that Stereo-SEM-DIC is needed for accurately characterizing fiber strain fields due to its curved surface. The effect of sputter coating on fiber tensile strength and strain is investigated via single fiber tensile tests. Results showed that there is no significant difference in the mean tensile strength and failure strain between uncoated and coated fibers (average increment in fiber diameter of \sim 221 nm due to coating) at 5% significance level. SEM images of failure surfaces for uncoated and coated fibers also confirmed a tensile failure of fibers as observed for polyacrylonitrile PAN-based fibers in literature.

1. Introduction

High performance carbon and glass fiber reinforced composites are widely used in aerospace, automotive, and defense applications. Longitudinal tensile failure of such composite systems mainly occurs when a cluster of single fibers break at characteristic length-scales in the range of few microns (~one fiber radius, $r \sim 2.6 \, \mu \mathrm{m}$ for carbon fiber) [1] to few hundred microns [2] (one ineffective length, $\delta \sim 10$ fiber diameters). Furthermore, it is known that fiber tensile strength is statistical in nature

due to the presence of defects, resulting in gage length (GL) dependent fiber tensile strength [3,4]. In general, single fiber tensile (SFT) testing at millimeter length-scales is used to characterize fiber strength distribution which is then extrapolated using Weibull distribution to determine strength at microscale. However, this often leads to over prediction of fiber strength at microscale which is required as an input for composite strength models [5]. A full fundamental understanding of strength performance of the fibers has been elusive and whether intrinsic strength follows a Weibull statistical distribution remains an open

a McNair Aerospace Center, University of South Carolina, Columbia, SC, USA

^b Department of Mechanical Engineering, University of South Carolina, Columbia, SC, USA

^{*} Corresponding author at: McNair Aerospace Center, University of South Carolina, Columbia, SC, USA *E-mail address:* sockalin@cec.sc.edu (S. Sockalingam).

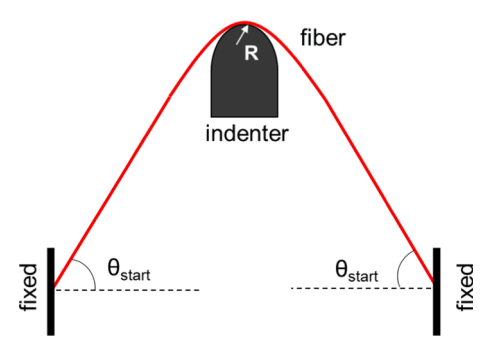


Fig. 1. Schematic of single fiber transverse loading experiment. (For interpretation of the references to colour in this figure legend, the reader is referred to the web version of this article.)

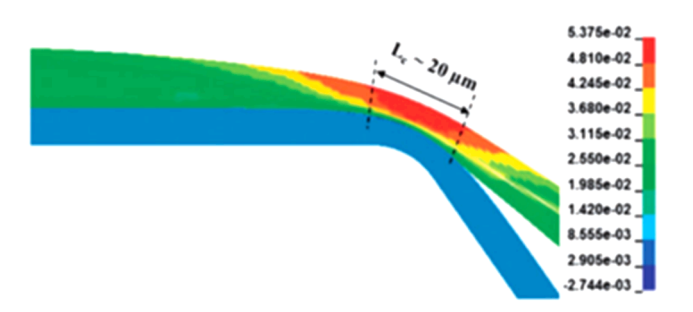


Fig. 2. Effective length over which axial strain concentration occurs for a Dyneema® single fiber transversely loaded via a fragment simulating projectile (R $\sim 20~\mu m$) [22]. (For interpretation of the references to colour in this figure legend, the reader is referred to the web version of this article.)

question. Hence, knowledge of accurate fiber tensile strength distribution at the characteristic microscale gage lengths is required to better understand the fundamental mechanisms governing fiber strength [6].

It is challenging to directly measure the tensile strength of fibers at such small characteristic length scales. The SFT test method cannot be used because clamping effects limit the smallest gage length that can be tested to 5 mm [7]. Single fiber fragmentation tests (SFFT) [4,8] allow testing of fibers up to a gage length of one ineffective length (~10 fiber diameters) as the fiber length becomes shorter with increasing number of fiber breaks. However, during longitudinal tensile failure of composites cluster of fiber breaks may occur at distances shorter than the ineffective length of the fiber as shown by the in-situ observation of longitudinal failure of T700/M21 carbon fiber epoxy composites by Swolfs et al. [1] and Scott et al. [9]. Thus, SFFT method may not be suitable for measuring fiber strength at gage lengths smaller than one ineffective length. Single fiber notch test [10,11] and loop [12] tests allow testing of fibers at microscale gage lengths due to stress localization around the notch and loop. However, the estimation of strength from these tests largely depends on the parameters used in the inverse analysis. Thus, there is a need for a method to directly measure the strength of the fibers at microscale gage lengths of failure.

The SEM-DIC technique [13–19] allows exploring deformations at extremely smaller length-scales. It involves capturing SEM images of the specimen surface as it deforms under applied loading. The SEM images are then correlated via commercial DIC software to measure specimen displacement and strain. An in-situ experimental technique based on the combination of transverse loading of single fibers under scanning electron microscope (SEM) with digital image correlation (DIC) is a potential approach to access characteristic microscale gage lengths $l_{ch,r} < l_{ch} < \delta$. Fig. 1 shows the schematic of a transverse loading experimental set-up adopted from Hudspeth et al [20]. They used such a set-up for studying the transverse failure of high-performance ballistic

fibers. A single fiber is clamped at its ends and transversely loaded using an indenter of a known geometry (tip radius, R). The starting angle (θ_{start}) and the tip geometry are both known to have effect on the levels of stress-concentration induced in the fiber-indenter contact region and the length over which the stress concentration is induced [21,22]. As reported in [22], axial strain in the fiber-indenter contact region is approximately two times higher (~5.4%) than the average tensile failure strain (2.4%) of Dyneema® fiber (diameter ~17 μm) transversely loaded using a fragment simulating projectile (FSP) of tip radius, R ~20 μm. And the length over which this strain (stress) concentration occurs was found to be approximately on the same order as the FSP tip radius, R, \sim 20 μ m as shown in Fig. 2 [22]. Using SEM-DIC technique, one can capture this strain concentration region at the fiber-indenter contact zone for the carbon fiber. Thus, we aim to use transverse loading experiments with different indenter tip radii and combine it with SEM-DIC technique to induce and measure stress-strain concentrations in single carbon fibers over length-scales observed during tensile failure of composites.

The use of SEM-DIC technique to measure local strain fields in individual single fibers requires a) a sub-microscale speckle pattern on the fiber surface and b) correction of spatial and time varying drift distortions caused by the SEM scanning process [14,18] and careful selection of SEM imaging parameters such as dwell time (tD), beam current, and image integration to improve signal to noise ratio in SEM images [15,18]. Dwell time (t_D) refers to the time spent by the electron beam at each pixel location to define its pixel intensity. Beam current is related to the number of electrons hitting the specimen surface and image integration involves taking multiple images scans and averaging them to reduce image noise. It is found that a longer dwell time and higher beam current with image integration generally results in less noise in SEM images [15,18]. The spatial and time varying drift distortions occurring in SEM images can induce artificial displacement fields in images which can result in large errors in displacement and strain fields measured by the DIC software. An SEM drift-distortion correction methodology is available in literature [14,18] to account for the spatial and drift distortions occurring in SEM and is employed in Section 3.2 for an in-situ SEM rigid body experiment. Along with optimal imaging conditions, as mentioned above the fiber surface also needs to have an isotropic, randomly distributed, and highly contrastive pattern on its surface for it to be accurately tracked by the DIC software [23]. There are a variety of methods for patterning specimens at small length-scales published in literature. An overview of patterning methods at nano-microscale can be found in [24,25]. Although there are several methods available for nanomicroscale pattern generation on polymer and polymer-based specimens, to the authors' knowledge there is very little published literature on pattern generation on delicate specimens such as cylindrical single fibers. Shafaqat et al. [25] recently developed a nanoscale patterning method specifically for fragile and delicate specimens such as a synthetic hydrogel fiber and a free-standing micro-tensile or highly stretchable MEMS specimen. It involved using a dry nebulized mist to pattern the specimen surface with one or a few nanoparticles at a time. They showed that features or speckles of size 50 nm-1 µm can be achieved using this method. However, an extensive experimental set up is required to use this technique and patterning via this technique can be time consuming. Other methods for patterning at microscale on polymer or polymerbased specimens include thin-film reconfiguration method [26,27], nanoparticle method using gold [28] or silica nanoparticles [29] to pattern the specimen surface, micro-stenciling [30], micro-stamping [31], focused-ion beam (FIB) [24,32,33], and electron beam lithography [24,34]. The advantages and disadvantages of using the methods listed above can be found in [25,35] in terms of the cost, patterning time, pattern quality and user application.

Because of the delicateness and tediousness of handling microscale single fibers, we need a faster patterning method that involves minimal steps, requires no surface modification, is less abrasive and does not cause any significant changes to fiber properties. A patterning technique

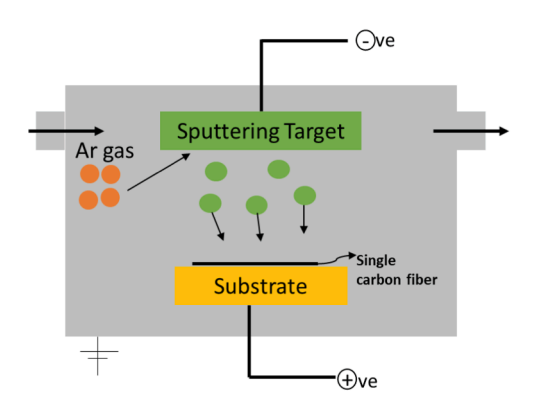




Fig. 3. a) Schematic for sputter coating of single fibers and b) sample inside Denton Vacuum sputter chamber. (For interpretation of the references to colour in this figure legend, the reader is referred to the web version of this article.)

that does not require surface modification is also important to study the effect of fiber sizing on tensile strength. Recently, Hoefnagels et al. [36] have shown the use of a one-step sputter deposition with indium-tin (In-Sn) alloy as a target material to generate patterns in the range of nanomicrometer length-scales by only varying the sputter-deposition conditions such as working pressure, current, and sputtering duration. They use a low melting temperature In-Sn solder alloy as a target material owing to its large adatom surface diffusion length to deposit the metal atoms in island growth mode from the start of deposition process. This alleviates the need for thin film re-arrangement or modeling for generating patterns from thin films deposited on specimens.

Therefore, in this study, we investigate the use of sputter-deposition to generate in one-step, a sub-microscale speckle pattern on single carbon fibers using a gold-palladium target. Various patterning conditions such as working pressure, sputtering current, and coating duration are used for generating patterns on the fiber surface. Numerical translation experiments are performed on the obtained patterns to study the effect of pattern noise and identify a suitable pattern for in-situ SEM-DIC experiments. An actual rigid body translation experiment is conducted inside the SEM using the best speckle pattern to perform a noise floor verification for SEM imaging. The effect of sputter coating on the fiber tensile strength is also investigated by performing tensile experiments on uncoated and coated fibers for the sputter coating condition that provided the best pattern. The best sputter coating condition is also used to pattern other single fibers such as unsized IM7 carbon fiber, Kevlar®, and Dyneema® fibers to investigate the applicability of the method to different fiber material systems.

2. Materials and methods

Sized and Unsized IM7 carbon fibers are acquired in the form of a spool of 12 K tow from Hexcel Corporation. The sized IM7 fiber had a proprietary 'GP' sizing and an average diameter of 5.2 μ m as specified in the Hexcel datasheet [37].

2.1. Pattern creation via sputter coating

A Denton Vacuum Desk II sputter coater without substrate temperature control is used to perform direct current sputter deposition on carbon fibers. Fig. 3(a) shows a schematic of the sputter deposition system. The deposition chamber consists of a target (material to be deposited) and substrate (single fiber specimen) which form the cathode and anode of the system, respectively. The deposition chamber is filled with Argon gas. When voltage is applied between the electrodes under vacuum conditions, target atoms are ejected by argon ions and accelerated towards the substrate where they condense to form a thin layer on the specimen surface [38,39]. The type of nanoparticle pattern formed

Table 1Sputtering conditions investigated for sized IM7 carbon fiber.

Condition	Current (mA)	Pressure (mTorr)	Duration (mins)
SC1	40	120-140	5
SC2	40	120-140	10
SC3	50	120-140	5
SC4	50	120-140	10
SC5	50	200	10

during sputter deposition depends on various deposition conditions such as sputtering current, working pressure or chamber pressure, the target and substrate material being investigated, and substrate temperature [40]. For SEM-DIC, we are mainly interested in nanoparticle feature size and high contrast of the pattern deposited on the substrate surface as they strongly affect the accuracy of image correlation. Therefore, we study the effect of varying deposition conditions such as sputtering current, working pressure, and sputter duration on the type of pattern generated on the fiber surface to determine a suitable pattern for our SEM-DIC experiments. Table 1 shows the conditions investigated for sputter deposition on sized IM7 fibers. A gold-palladium (Au-Pd) target is used to initially investigate pattern creation on single fibers as it is one of the commonly used alloys for sputter deposition. Single fibers are extracted from the tow and mounted on aluminum stubs using a carbon sticky tape for sputter coating (Fig. 3(b)). All the sputter deposition is performed at room temperature. The coated fibers are then imaged by a Zeiss Gemini FE500 SEM with the following conditions: an Everhart-Thornley secondary electron detector, an accelerating voltage of 5 kV, beam or probe current of 200nA, dwell time (tD) of 12.8 µs, a working distance of 5–7 mm, a field-of-view of ${\sim}4~\mu m \times 3~\mu m$ (magnification- \sim 25000x-35000x), and a recording resolution of 1024 \times 768 pixels (pixel size ~4 nm/pixel). It must be noted here that only single image scan is used to obtain the pattern images shown in Fig. 4. Line integration (using 8 scans) to reduce rastering noise is only used for SEM drift-distortion correction procedure in Section 3.2. The said accelerating voltage of 5 kV was used to limit damage to the fiber caused by the electron beam when imaging the fiber for extended periods during SEM-DIC experiments. A similar accelerating voltage has also been used by Montogomery et al. [41] for SEM-DIC experiments on single glass fiber/ epoxy and carbon fiber/epoxy composites with reconfigured Ag thin films. They also report that the use of a dwell time of $\sim 10~\mu s$ for imaging their specimens resulted in lowest image noise. A working distance of 5–7 mm is determined as best via trial and error for observing the submicroscale Au-Pd pattern on the fiber surface.

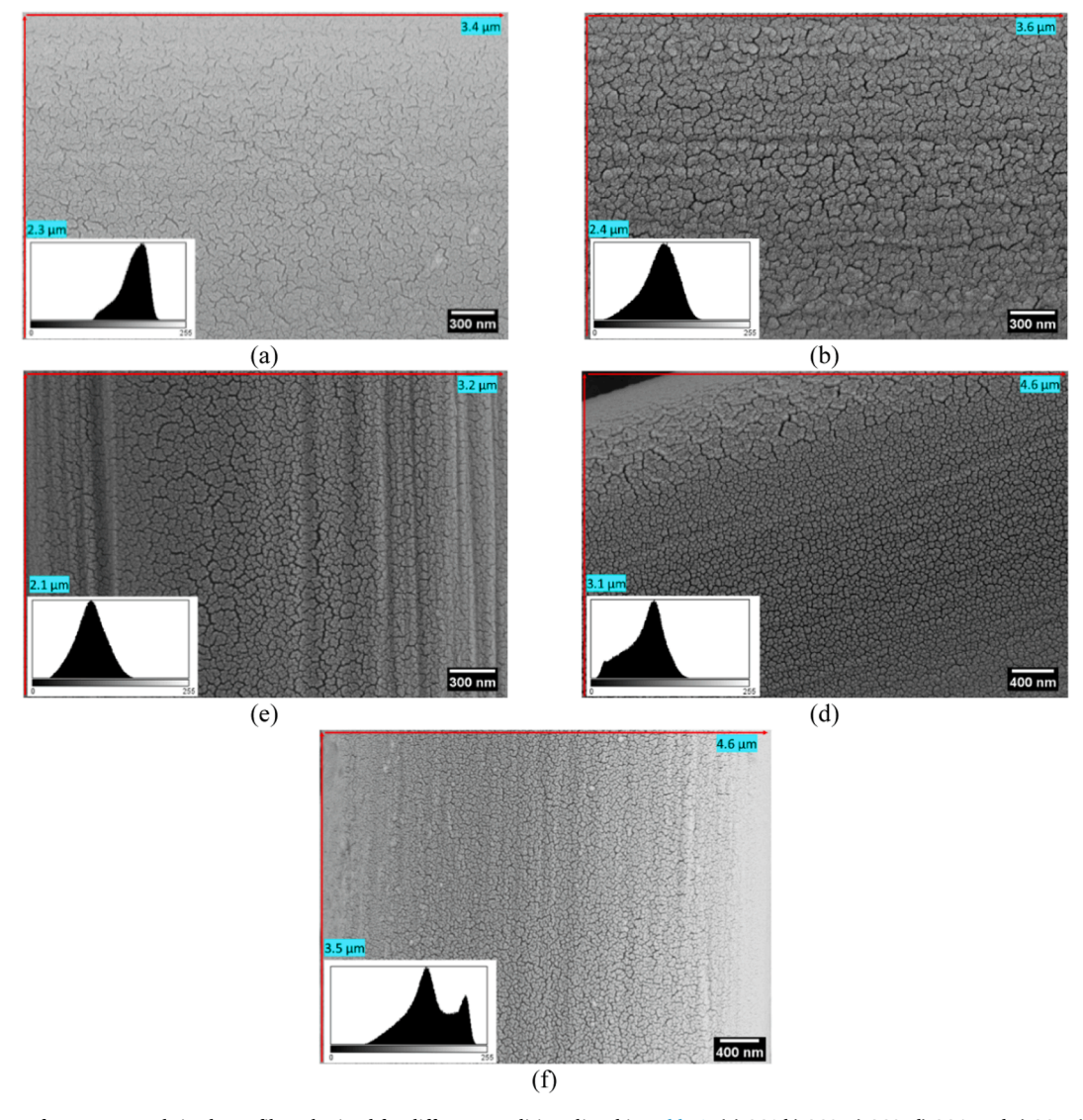


Fig. 4. SEM images of sputter coated sized IM7 fiber obtained for different conditions listed in Table 1. (a) SC1 b) SC2, c) SC3, d) SC4, and e) SC5. (For interpretation of the references to colour in this figure legend, the reader is referred to the web version of this article.)

3. Results

Fig. 4(a)-(e) shows the SEM images of the patterns formed on the fiber surface for the sputter coating conditions listed in Table 1. Comparing Fig. 4(a), (b), and 4(c), (d) respectively, shows that an increase in sputter coating duration for the same sputtering current results in formation of a greater number of nanoclusters of Au-Pd particles on the fiber surface. Increasing sputtering current for the same duration of coating (Fig. 4(a), (c) and Fig. 4(b), (d)) results in patterns with welldefined boundaries or dark regions, separating the nanoclusters. Similar nanocluster patterns as those observed in Fig. 4(a)-4(c) are also reported by Tanaka et al. [42] for gold particles deposited on an IM600 carbon fiber polymer matrix composites. They used the nanocluster pattern to study the localized deformation of a composite subjected to three-point bending. From the patterns shown in Fig. 4, only the patterns shown in Fig. 4(d) and 4(e) exhibit a higher proportion of smaller individual nanoclusters with well-defined boundaries. It is also important to note that the pattern in Fig. 4(e) consisting of densely packed nanoclusters is obtained at a higher working pressure of 200 mTorr whereas the other patterns are obtained at a lower working pressure of 120 mTorr. This is done to investigate the effect of pressure on the size of nanocluster formed on the fiber surface, as higher working pressures are

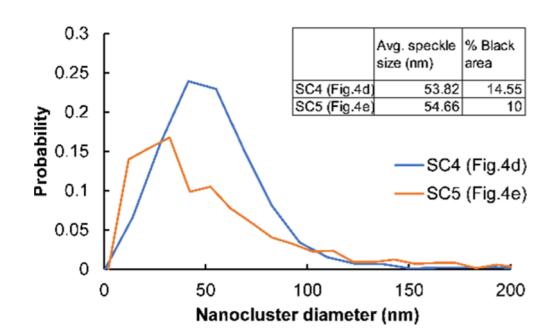


Fig. 5. Nanocluster diameter distribution. (For interpretation of the references to colour in this figure legend, the reader is referred to the web version of this article.)

linked to smaller feature sizes in the work of Hoefnagles et al. [36].

To obtain an estimate of the speckle/feature (cluster) sizes in patterns of Fig. 4(d), and 4(e) particle analysis is performed using the image processing toolbox in MATLAB. A similar particle analysis has been performed by Montgomery et al. [27] to find the size of nano-islands after performing thin film reconfiguration of the top Ag film on the

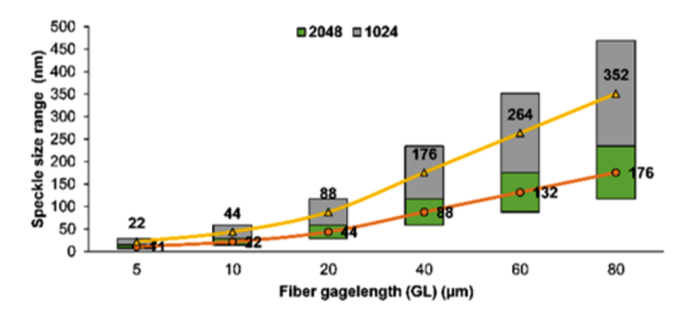


Fig. 6. Ideal range of speckle size versus gage length for different image recording resolution. (For interpretation of the references to colour in this figure legend, the reader is referred to the web version of this article.)

Ag-Ti-Au-Ti stack. Otsu's method [43] is used for thresholding the pattern. A morphological opening operation is then used to remove the noisy pixels at the boundaries of the nanoclusters. The equivalent diameter (d_{eq}) of each nanocluster is obtained as the diameter of circle having the same area as the nanocluster, computed as shown in Equation (1).

$$d_{eq} = \sqrt{\frac{4*Areaofnanocluster}{\pi}} \tag{1}$$

Fig. 5 shows the nanocluster size distribution for both the patterns along with their mean cluster size. Average nanocluster size obtained for both patterns SC4 (Fig. 4d) and SC5 (Fig. 4e) is similar, approximately of size \sim 53–54 nm, although pattern SC5 was deposited at a slightly higher pressure. An ability to better tune the working pressure over a wider range using a turbo-pump sputter coater is probably required to observe the influence of pressure on deposited pattern as observed by Hoefnagels et al. in their study [36]. Also, the nanocluster size distribution is slightly skewed for pattern SC5 compared to pattern SC4 which has a more Gaussian or bell-shaped type distribution of nanoclusters.

Subset-based DIC guidelines suggest that speckle or feature sizes (FS) should be no smaller than the range of 3 pixels < FS < 6 pixels for optimal accuracy and each subset or correlation window must contain at least 3 such speckles across it [23]. This is because smaller speckles (speckle size < 3 pixels) are prone to aliasing and larger speckles (speckle size > 6 pixels) limit the spatial resolution in measurement from image correlation. Based on this guideline, the ideal range of speckle (nanocluster) sizes in nanometers can be calculated for viewing a desired length or width of the object at a given recording resolution using Equation (2).

$$FS(in \ nm) = FS(in \ pixels) * \frac{Length \ of \ object \ to \ be \ viewed(nm)}{recording \ resolution}$$
 (2)

Fig. 6 presents a column chart for ideal speckle size vs fiber gage length for two recording image resolutions of 1024×1024 pixels and 2048×2048 pixels. As shown in Fig. 6, the ideal speckle size range increases with increase in fiber gage length. This trend is shown by a line curve passing through the center of each of the columns for both recording resolutions. The mid-point value for the range of speckle sizes for both recording resolutions is also denoted on the curve. Fig. 6 also shows that increasing the recording resolution, allows accessing longer gage lengths for a given average speckle size in nm. For example, pattern SC4 consisting of nanoclusters of average size $\sim\!53$ nm, is suitable for correlating fiber gage lengths in the range 9 $\mu m < GL < 17.7$ μm and 17.7 $\mu m < GL < 35.5$ μm for recording resolutions of 1024×1024 pixels and 2048×2048 pixels, respectively.

Another important parameter that plays a significant role in achieving good image correlation is pattern contrast. An ideal speckle pattern contains approximately equal distribution of bright and dark regions which results in good contrast for accurate subset matching and displacement measurement [23]. A characteristic feature of all the

patterns shown in Fig. 4 is that the pixel intensity distribution (shown as inset in Fig. 4) of all patterns is dominated by brighter pixels. It is possible to calculate the percentage of dark pixels and their distribution using a similar particle analysis technique mentioned above for determining the size of nanoclusters. Fig. 5 also shows the percentage of black pixels for patterns SC4 and SC5. Pattern SC4 has a slightly higher percentage (14.5%) of black pixels than pattern SC5 (10%), which generally corresponds to improved contrast for image correlation.

3.1. Numerical experiments for pattern assessment

In this section, to assess the suitability of the obtained patterns for DIC, we perform numerical rigid body translation experiments and study image correlation. Several researchers have used such a method in literature [44-46] for assessing pattern quality and for quantifying errors in DIC [47] without having to perform physical experiments which can be time and cost intensive. This is usually done by employing the fast Fourier transform algorithm (FFT) as it is known to generate the least error in sub-pixel translation of images, provided the shift is applied correctly in the Fourier or frequency domain. Here, we use a method reported by Reu et al. [48] which employs the FFT algorithm to perform numerical translation of images. We assume the surface of the fiber to be flat and use the 2-D pattern images shown in Fig. 4 for numerical translation. Our aim is to perform numerical experiments to investigate the influence of pattern image contrast of the obtained patterns on image correlation to help identify a suitable pattern that can be used for in-situ SEM experiments. The pattern with the best correlation performance is then used in Section 3.2 for SEM rigid body experiments for SEM drift/distortion correction. Each pattern shown in Fig. 4 is first converted to frequency domain by performing a row-by-row Fast Fourier transform (FFT). A linear phase shift is then applied in the frequency domain with the amount of phase shift corresponding to the desired subpixel shift or translation. The image is then converted back to the spatial domain by performing an inverse FFT. Using the method described above, translated image pairs are generated for each pattern in Fig. 4 by applying sub-pixel 'u' displacements in the x-direction in the range of 0-1 pixel with an increment of 0.1 pixel between images. A constant zero mean Gaussian noise with a variance of 4 grey-levels is also added to the translated images. The translated images are then analyzed using a commercial DIC software VIC-2D for correlation.

In DIC analysis, subsets, or small virtual windows within the area of interest (AOI) are compared between the reference and deformed images during correlation. For any given FOV, the minimum subset size required for accurate correlation is given by 3*speckle size. A brief investigation into the effect of subset size on correlation is discussed below for the pattern that leads to the least error in displacement.

Fig. 7(a) shows the mean displacement error against the applied displacement 'u' for the different patterns for a subset size of 61x61 pixel², step size of 2 pixels, normalized 8-tap interpolation scheme. Mean displacement error is calculated as the difference between the DIC-calculated average displacement within the area of interest and the applied displacement, 'u'. The AOI is chosen as the entire region of the fiber under the field of view barring the edges of the image as shown in Fig. 7(e). Fig. 7(e) also depicts the reference subset size of 61x61 pixel² $(\sim 0.192 \times 0.192 \, \mu m^2)$ used for correlation. A larger subset size of 61×61 pixel² is initially chosen to improve subset matching as the patterns have a low contrast, having a higher proportion of gray intensities than black intensities. Normalized 8-tap interpolation scheme is chosen for performing correlation based on the results of numerical translation studies performed by Reu et al. [48] which showed that compared to bicubic, 4tap, and 6-tap interpolation schemes, the 8-tap interpolation scheme resulted in the least mean displacement error.

As seen from Fig. 7(a), the smallest mean displacement error is obtained for the pattern SC4 (Fig. 4d) followed by the pattern SC1 (Fig. 4a). Here, SC4 refers to the sputter coating (SC) condition (4) listed in Table 1. Patterns SC2 (Fig. 4b), SC3 (Fig. 4c), and SC3 (Fig. 4e) show

K. Shah et al.

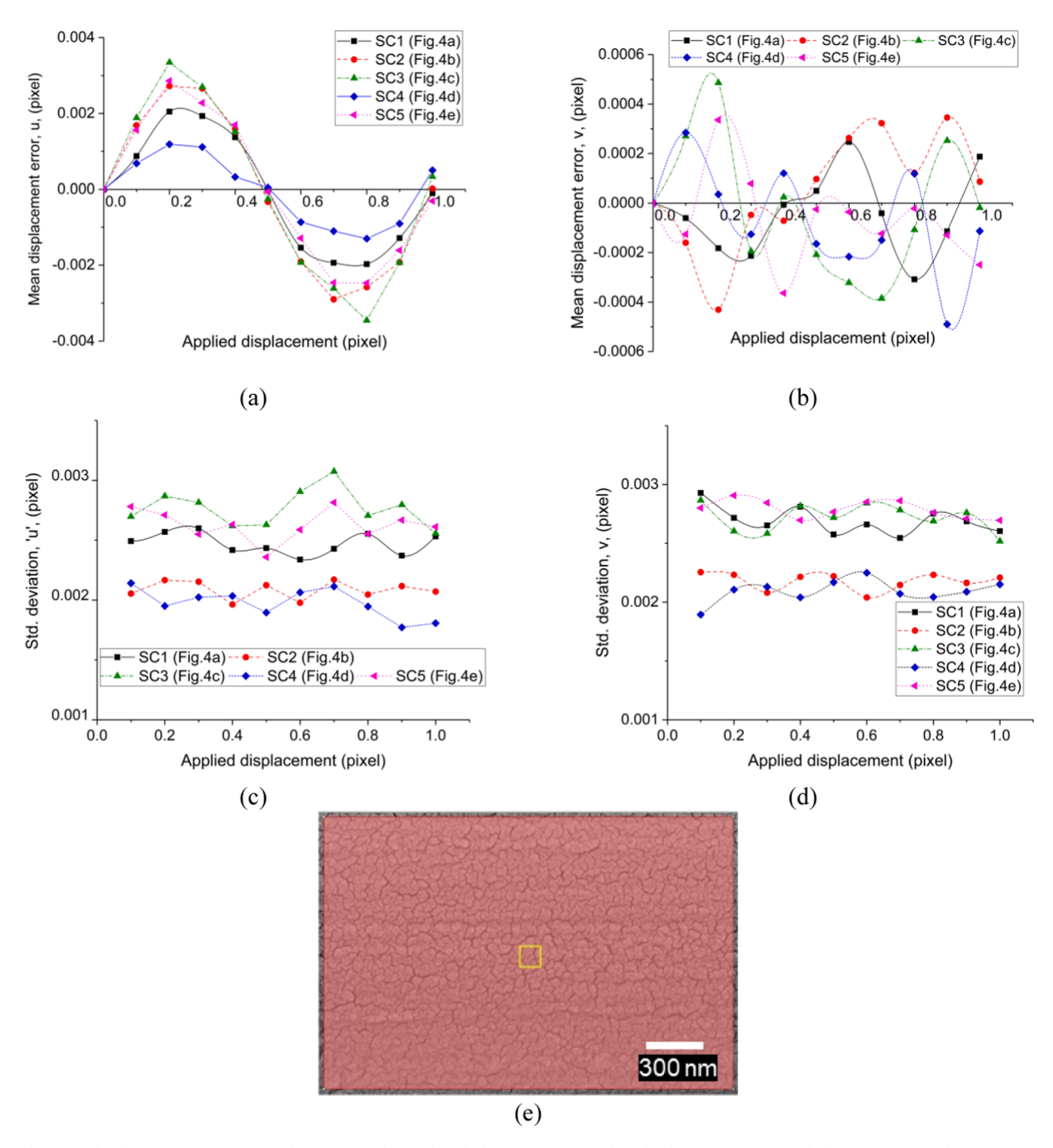
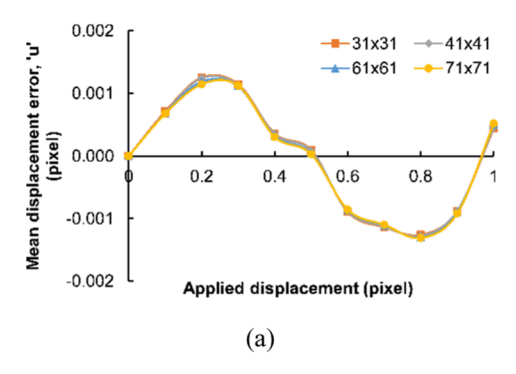


Fig. 7. a), b) Mean displacement error in 'u' and v respectively, c), d) Std. deviation in 'u' and 'v' displacement respectively for sputter coated patterns in Fig. 4, and e) example AOI and subset size (61x61 pixel²) used. (For interpretation of the references to colour in this figure legend, the reader is referred to the web version of this article.)

approximately similar trend in their mean displacement errors. It is also noted that the mean displacement error graph shown in Fig. 7(a) is consistent with the pioneering work of Schreier et al. [49], where the authors for the first time showed that the source of the mean displacement error is the intensity interpolation method. The standard deviation in the measured 'u' displacement is presented in Fig. 7(c) for the different patterns. For all patterns, the standard deviation in 'u' displacement is approximately constant with the lowest standard deviation observed for the pattern SC4. Mean displacement error in 'v' for applied displacement in 'u' is shown in Fig. 7(b). For all the patterns the mean displacement errors in 'v' are nearly random in nature and one order lower than the mean displacement error in 'u'. The standard deviation in 'v' is comparable to standard deviation measured in 'u'

displacement for all the patterns as shown in Fig. 7(d). The effect of subset size on the correlation error and standard deviation in displacement is shown Fig. 8 for pattern SC4. As seen from Fig. 8, there is negligible change in the mean displacement error with increasing subset size, however, the standard deviation in 'u' measurement reduces by half going from a small subset size of 31x31 pixel² to large subset size of 61x61 pixel² an observation that is consistent with previous studies [13] that showed averaging over larger subsets reduces the effect of intensity pattern noise, at the expense of reducing spatial resolution. Overall, the results from Figs. 7 and 8 indicate that pattern SC4 may be the most suitable candidate for our future in-situ SEM experiments and that a larger subset size may be required for pattern SC4 to obtain better results due to an overall low pattern contrast. Additional experiments would be



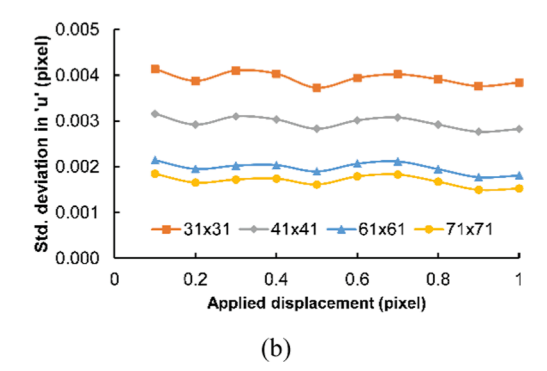
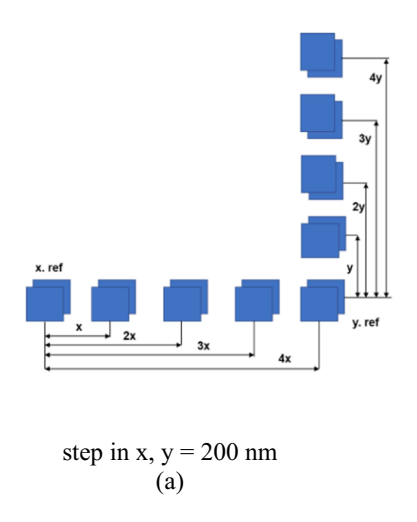


Fig. 8. Effect of subset size on a) mean displacement error and b) standard deviation in 'u' for different subset sizes for pattern SC4. (For interpretation of the references to colour in this figure legend, the reader is referred to the web version of this article.)



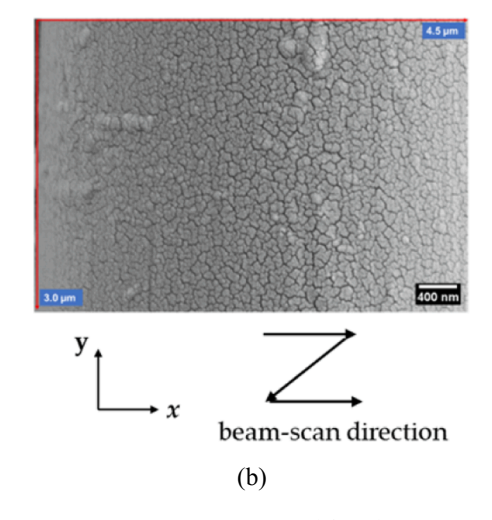


Fig. 9. a) 'L' shaped motion [18], and b) Patterned IM7 fiber used for drift distortion correction. (For interpretation of the references to colour in this figure legend, the reader is referred to the web version of this article.)

required to determine the subset size and minimum possible spatial resolution in measurement based on the displacement or strain field that needs to be measured for a given FOV and speckle pattern.

3.2. Rigid body experiment for SEM drift-distortion correction

SEM imaging introduces two major types of noise in the images in the form of spatial and drift distortions [14,18]. Spatial distortion are distortions associated only with pixel positions in image such as those encountered by any imaging device. Drift distortions are time varying distortions caused by electron beam scanning process of SEM which induce an 'apparent' displacement of pixel locations with time. Such distortions were not considered in the numerical translation experiments presented in Section 3.1. In this section, we use the SEM driftdistortion correction procedure established in literature [14,18] to investigate and correct for the spatial and drift distortions encountered during SEM imaging. A sized IM7 single fiber is coated using the best patterning condition (SC4) identified from the above analysis. Images of the pattern are taken incrementally as it is translated stepwise, step size = 200 nm, in x and y directions inside an SEM using the motorized SEM stage to create a 'L' shaped motion as shown in Fig. 9(a). At each translation step, two images are acquired, and their corresponding acquisition time are recorded for drift correction. The orthogonal 'L' shaped motion is used to correct for spatial distortion using the known largest displacement in x and y. All pattern images are acquired at a working distance - 7.5 mm, magnification ~25000x (4.4 nm/pixel), dwell time (t_D) - 12.8 µs, and using 8x line integration to reduce

rastering noise [14–16,41] resulting in a total frame time (t_F) of 80.8 s. SEM drift-distortion analysis is performed using commercial correlation software VIC-2D using a subset size of 61x61 pixel² and a step size of 2.

Fig. 9(b) shows the patterned fiber reference image used for the SEM drift distortion analysis. For the SEM-magnification level (~25000x) considered in this study, spatial distortions are expected to be significantly lower compared to drift distortion which become more dominant with increasing magnification [14,16,18]. The measured drift displacement fields at time $t \cong 24$ mins, are shown in Fig. 10(a). The time $t \cong 24$ mins is the time of image capture for the fifth translation step (t = 0 mins, at the start of the experiment). Fig. 10(b) shows the measured spatial distortion field. The measured spatial distortion fields are surprisingly larger than the drift distortion field in both x and y directions by up to \sim 1.5x and 6x respectively. Also, the spatial distortion fields shown in Fig. 10(b) are uniform in nature compared to the nonuniformly varying distortion fields observed in literature [16,18]. Ideally, after drift/spatial distortion correction using the procedure described, strains measured from image correlation for rigid body motion of the specimen should be close to zero except for some random noise from image acquisition. However, the strains obtained from the rigid body translation experiment performed above as shown in Fig. 11 are significantly higher than expected. The 'y' axis in Fig. 11 is shown as strain error in comparison to zero strains expected in the specimen. Mean error (bias) and standard deviation (noise) in strain are also shown in Fig. 11 for both x and y directions. As seen from Fig. 11, ε_{xx} has a lower mean error (~200-400 µstrain) or bias but comparatively higher standard deviation or noise which increases monotonically with each

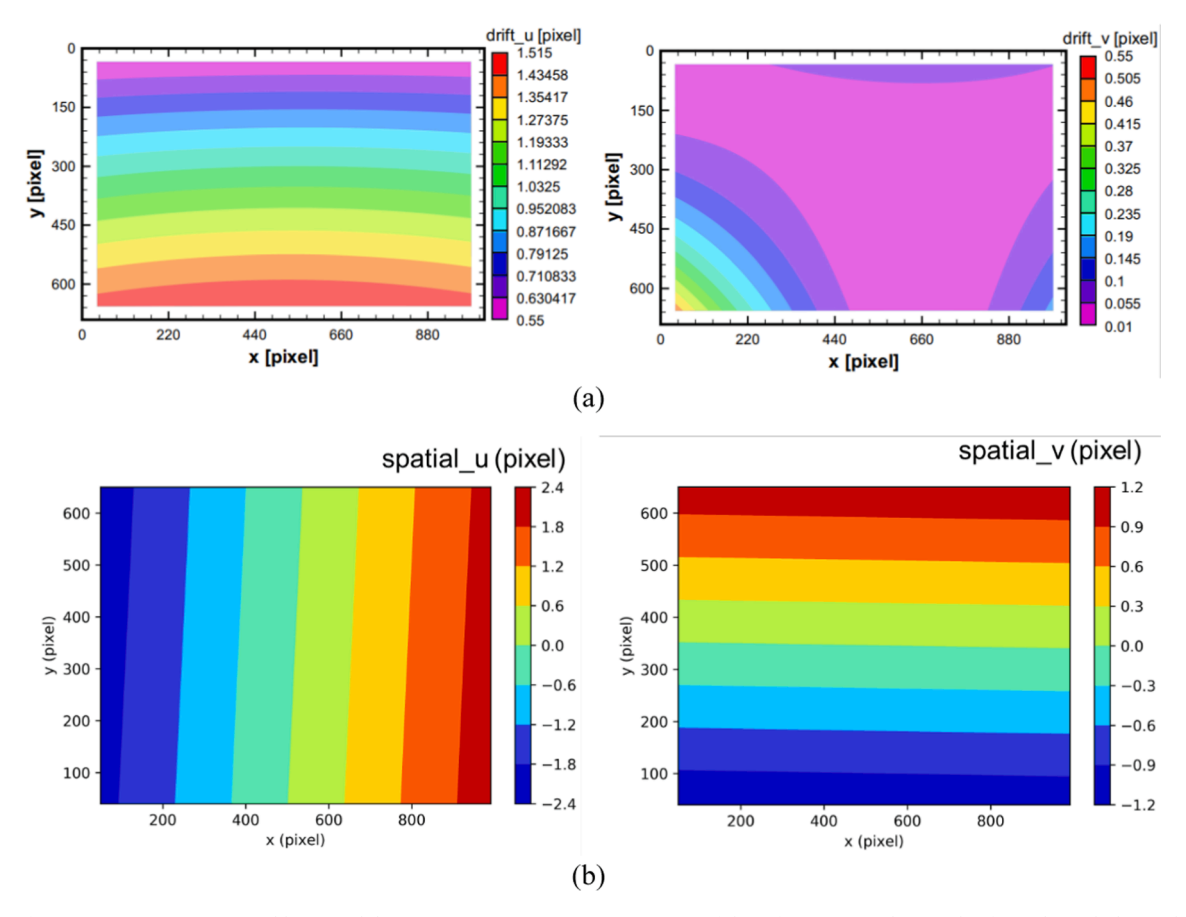


Fig. 10. a) Drift contours at $t \approx 24$ mins and b) Spatial distortion contours. (For interpretation of the references to colour in this figure legend, the reader is referred to the web version of this article.)

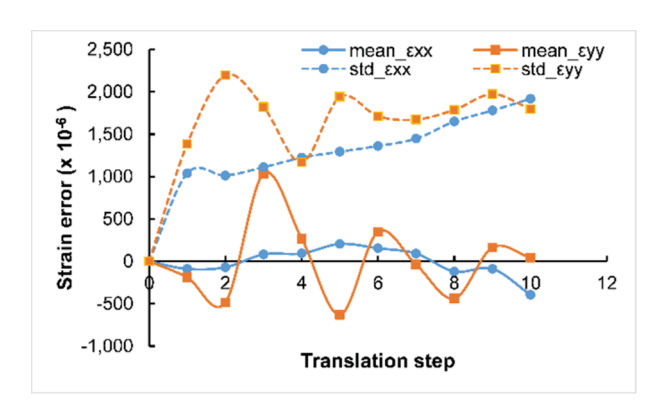


Fig. 11. Mean error (bias) and standard deviation (error) in strain measurements from rigid body translation experiment. (For interpretation of the references to colour in this figure legend, the reader is referred to the web version of this article.)

translation step to approximately $\sim\!2000$ µstrain. ε_{yy} is fluctuating in nature and displays a significantly higher bias ($\sim\!1000$ µstrain) and noise level of $\sim\!2000$ µstrain when compared to ε_{xx} .

A higher bias and noise in ε_{yy} compared to ε_{xx} could be an effect of rastering error during an SEM scan, wherein the distance between two rows as the beam moves from one row to the next on the specimen is not constant. Therefore, higher errors in strain are generally expected in a direction perpendicular to that of the beam scan as shown in Fig. 9(b) [14–16,41]. Performing line integration or line averaging while acquiring images (as done here), helps in smoothing out this error

[14–16,41] and such high levels of bias and noise observed for ε_{vv} as depicted in Fig. 11 is not expected. The large bias and noise levels observed in ε_{xx} and ε_{yy} are thought to be caused by projection of a curved fiber surface (3D) onto a 2D image plane. This can be observed from the strain contours, ε_{xx} and ε_{yy} , at different displacement steps as shown in Fig. 12. As the pattern is translated in x, only a smaller area near the center of the FOV (marked by the blue lines) depict relatively low strains (see Fig. 12(a)). Strains become increasingly larger moving away from the center and towards the edges as the curvature of the fiber becomes more prominent. It must also be noted that FOV becomes smaller between step 1 and step 5 as some portion of the patterned fiber moves out of the FOV with translation. For both translation steps, ε_{yy} strains are significantly higher than ε_{xx} across the entire FOV. The horizontal bands of strain depicted for ε_{vv} (Fig. 12(b)) are an effect of the rastering error, and the high levels of noise associated with it are attributed to the fiber curvature. Although the measured noise levels for ε_{xx} and ε_{yy} are approximately one order lower, 0.2% (~2000 µstrain) than the nominal fiber failure strain of ~2%, the projection errors can significantly increase with specimen deformation during an actual test and mask the actual specimen strains with noise. Thus, 2D-DIC technique has limitations when considered for a curved fiber specimen due to high levels of noise in strain measurement. Three dimensional DIC (3D-DIC) or StereoDIC is needed for accurate mapping and measurement of the 3D fiber surface.

Zhu et al. [17] have reported such a 3D-DIC method using SEM where multiple images of the specimen are taken by tilting the specimen stage. The StereoSEM procedure requires taking images of a calibration grid at at least two angles to establish the stereo imaging parameters for 3D-DIC and correct for SEM drift/distortion in images. Using the said procedure, the authors showed reduction in errors in out of plane

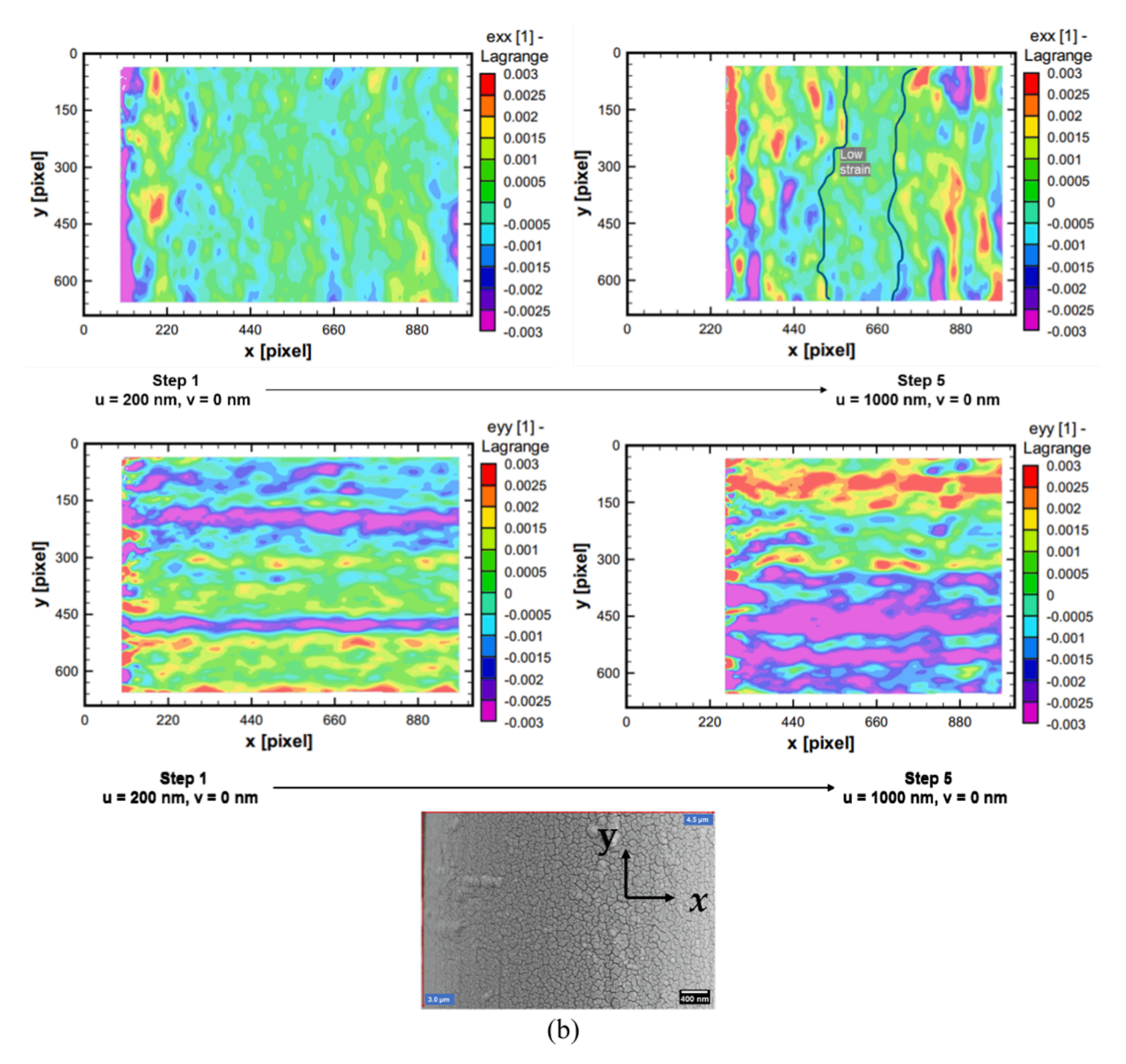


Fig. 12. Strain contours a) ε_{xx} , and b) ε_{yy} at two rigid body displacements of u=200 nm and u=1000 nm. (For interpretation of the references to colour in this figure legend, the reader is referred to the web version of this article.)

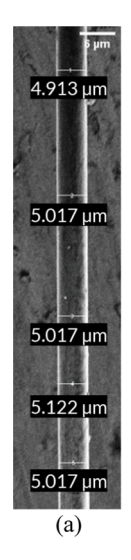
translation (0.1 mm) and out of plane rotation (2) to approximately a few hundred micro-strains. Otherwise, the errors from out of plane translation and rotation are on the order of few thousand micro-strains. These errors are on the same order as we obtain from 2D-DIC for our curved (3D) fiber specimen that has variations in its 'z' dimension and is comparable to having an out of plane translation of the specimen. An investigation into the use of this method for SEM drift/distortion correction analysis is a part of our future research and is outside the scope of the current study.

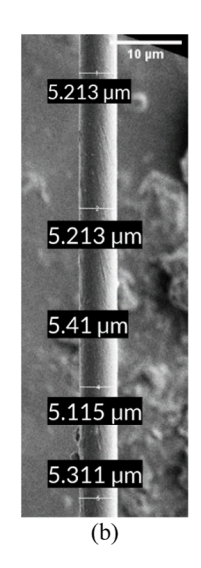
3.3. Effect of sputter coating on fiber tensile strength

The pattern deposited on the fiber surface via sputter coating must not cause damage to the fiber and alter its mechanical properties. Thus, the effect of patterning method on fiber strength is investigated using single fiber tension tests of coated and uncoated fibers. As a preliminary investigation into the effect of coating on fiber strength, only the best sputter coating condition {50 mA, 100 mTorr, 10 mins (current, working pressure, duration)} is considered for this study. Fiber diameter of uncoated and coated specimens are also measured using SEM images of

fibers taken before testing. These images are taken at a working distance of 31 mm and a magnification of 1000X using the Zeiss Gemini FE 500 SEM. Images of uncoated and coated fibers are then processed using ImageJ software to measure the fiber diameter by taking an average of the diameter measured at five different locations along the fiber length as shown in Fig. 13(a) and 13(b). Table 2 shows the average diameter comparison of uncoated and coated fibers measured across 21 specimens.

As seen from Table 2, there is an average increase in diameter of 221 nm for the coated fibers. Table 2 also presents the results of a paired samples t-test for fiber diameter at 5% significance level. The null hypothesis and alternative hypothesis are taken as follows: a) null hypothesis: no difference in the fiber diameter due to coating, and b) alternate hypothesis: fiber diameter is different for uncoated and coated configurations. The t-statistic and the standard error parameters needed for a paired samples t-test are calculated as shown in Equations (3) and (4). The t-critical value obtained at 5% significance level and number of degrees of freedom equal to 18 (# specimens – 1) is 2.101. The t-statistic value obtained using Equation (1) is 3.16. Since the t-statistic t-critical we reject the null hypothesis concluding that sputter coating results in





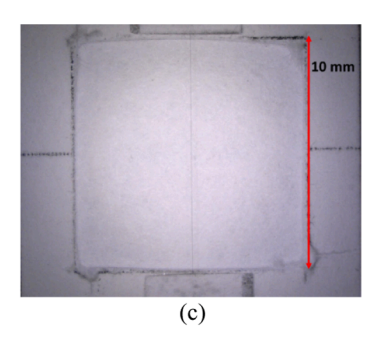


Fig. 13. Diameter measurement of a) uncoated and b) sputter-coated fibers and c) windowed paper template used for tensile testing. (For interpretation of the references to colour in this figure legend, the reader is referred to the web version of this article.)

Table 2Average change in diameter between coated and uncoated sized IM7 fiber.

	Average diameter (µm)
Uncoated fiber	5.179
Coated fiber with modified diameter after coating	5.40
Coated fiber with original diameter before coating	5.21
t-statistic, t-critical (5%)	3.16, 2.101
# dof	18

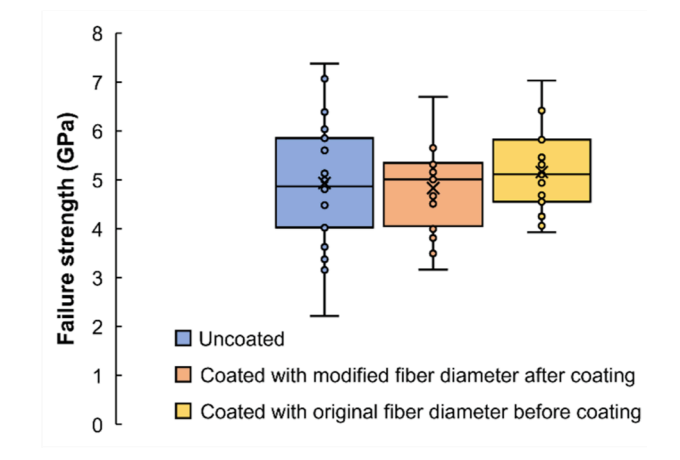


Fig. 14. Box and whisker plot of fiber tensile strength. (For interpretation of the references to colour in this figure legend, the reader is referred to the web version of this article.)

an increase in diameter of the fibers.

$$t = \frac{x_{diff}}{s_{\bar{x}}} \tag{3}$$

$$s_{\bar{x}} = \frac{s_{diff}}{\sqrt{n}} \tag{4}$$

The effect of sputter coating on fiber tensile strength is then studied by performing tensile tests of the coated and uncoated fibers. Sputter coated fibers from the above study of gage length 10 mm are mounted on a windowed paper template using cyanoacrylate glue as shown in Fig. 13 (c). The template is gripped at the edges of the window using serrated wedge grips and tested in tension according to the ASTM standard

Table 3Average fiber tensile strength for uncoated and coated fibers.

	Uncoated fiber	Coated fiber (with modified fiber diameter after coating)	Coated fiber (with original fiber diameter before coating)
Avg. strength (GPa)/ Std. deviation	4.935/ 1.277	4.832/0.872	5.158/0.817
# Specimens	21	19	19

C1557 [50] on an INSTRON Model 5944 Single Column Tester using a 10 N load cell at a displacement rate of 8 $\mu m/s$. A separate baseline tensile tests of uncoated fibers is also performed using the same gagelength and method as described above for comparison.

Fig. 14 shows a box and whisker plot of fiber tensile strength obtained from the tensile tests of uncoated and coated fibers. Fiber tensile strength is calculated as $F_f/(\pi d^2/4)$, where F_f is the force at failure, d is fiber diameter measured from SEM images. For the coated fiber, tensile strength is calculated using both the original fiber diameter before coating and the modified final fiber diameter after coating as shown in Fig. 14. This is done to investigate whether the change in diameter due to coating has a significant effect on fiber strength by conducting two independent sample t-tests as described later. The mean tensile strength is shown by a cross in each plot in Fig. 14 and is also listed in Table 3. The slight decrease in the mean fiber strength observed for coated fibers is likely an effect of increase in fiber diameter due to coating, and hence the cross-sectional area used for calculating fiber tensile strength. Furthermore, the measured mean strength for both uncoated (4.94 GPa) and coated fibers (4.83 GPa) is approximately 14-18% lower compared to the strength of \sim 6.0 GPa reported by Lyons et al. [51] for an IM7 single fiber of gage length 10 mm. This could be the effect of low sample size of both coated and uncoated specimens, presence of clamp effects, and some handling damage caused to the fibers while extracting them from the tow for tensile testing. The average failure strain for both uncoated and coated fibers is 0.0167 ± 0.004 and 0.018 ± 0.003 respectively. It must be noted here that the said failure strains are not corrected for machine compliance. In the future we plan to measure machine compliance for accurate strain calculations and comparison of failure strains between uncoated and coated fibers.

Two independent sample t-tests at 5% significance level are conducted to determine whether the difference in tensile strength observed between coated and uncoated fibers is statistically significant. T-tests are

Table 4 Independent samples *t*-test.

# Degrees of freedom	t-critical at 5%	t-statistic
38	2.032	0.293 uncoated vs coated fibers with modified fiber diameter after coating 0.637 uncoated vs coated fibers with original fiber diameter before coating

conducted for strength data between a) uncoated and coated fibers with strength values for coated fibers calculated using the modified fiber diameter after coating, and b) uncoated and coated fibers with strength values for coated fibers calculated using original fiber diameter, i.e., fiber diameter before coating. The null hypothesis is taken as no difference in the mean values of strength between coated and uncoated fibers ($\mu_{coated} = \mu_{uncoated}$). The alternate hypothesis is then that the mean fiber strengths for coated and uncoated fibers are different ($\mu_{coated} \neq \mu_{coated} \neq \mu_{coa$

 $\mu_{uncoated}$). A two-tailed *t*-test at 5% significance level is conducted with the population variances assumed to be the same $(\sigma_1^2=\sigma_2^2)$. The value of the t-statistic and number of degrees of freedom are calculated using Equations (5) and (6). Table 4 presents the calculated parameters including t-critical, t-statistic, and number of dof (degree of freedom) for the *t*-test calculated using Equations (5) and (6). Since t-statistic < t-critical for mean strength for both test cases (a) and (b), we accept the null hypothesis and conclude that at 5% significance level there is no difference in the mean fiber strength of coated and uncoated fibers. Although, this is in line with our expectation of the patterning method having a negligible effect on fiber properties, the sample size investigate in the above study was limited to 19–21 specimens. A larger sample size of coated and uncoated fibers may be required to reach a more accurate conclusion.

$$t = \frac{\mu_1 - \mu_2}{s_p \sqrt{\frac{1}{n_1} + \frac{1}{n_2}}} \tag{5}$$

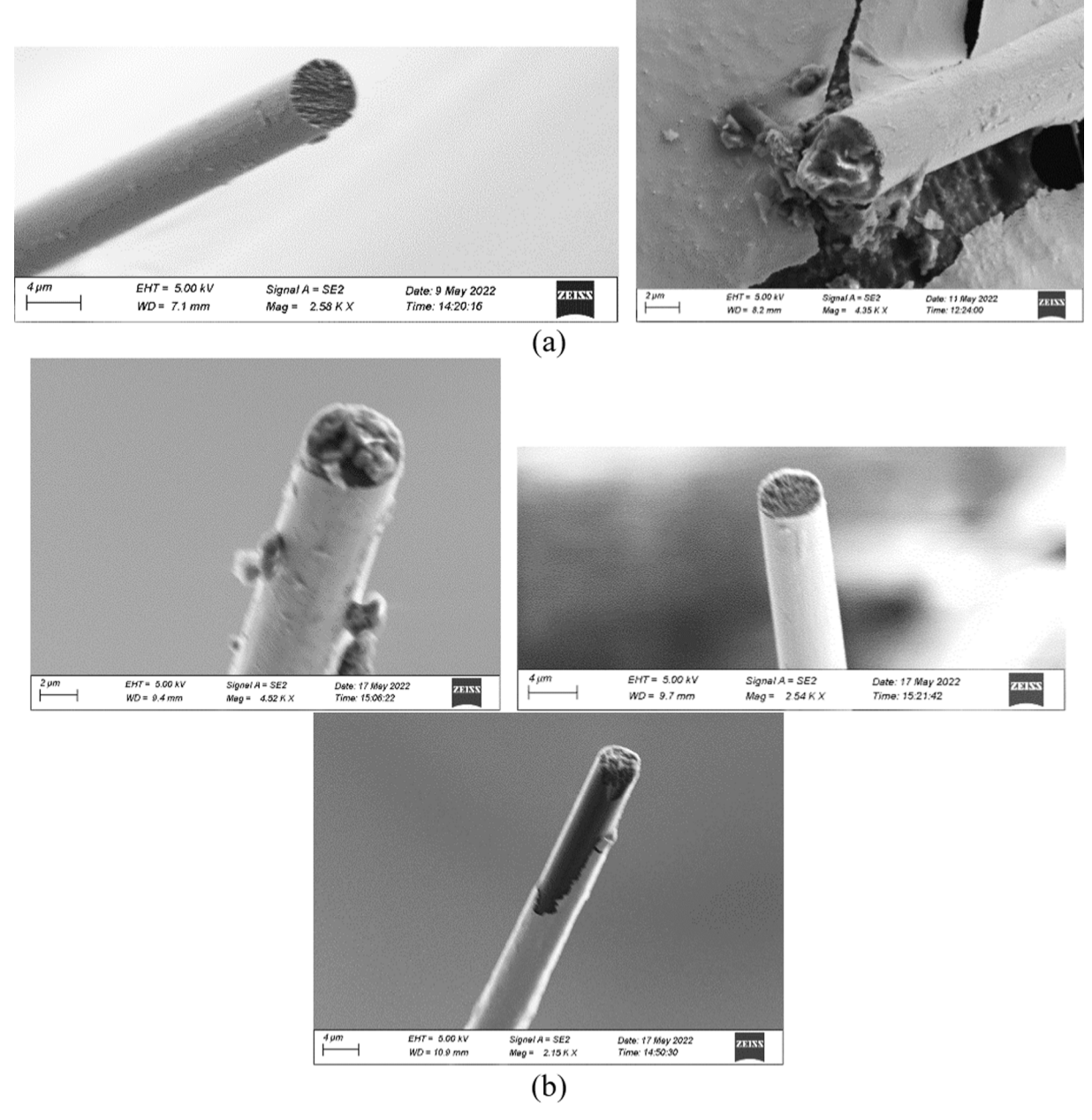


Fig. 15. Failure surfaces of a) uncoated fibers and b) coated fibers after tensile testing.

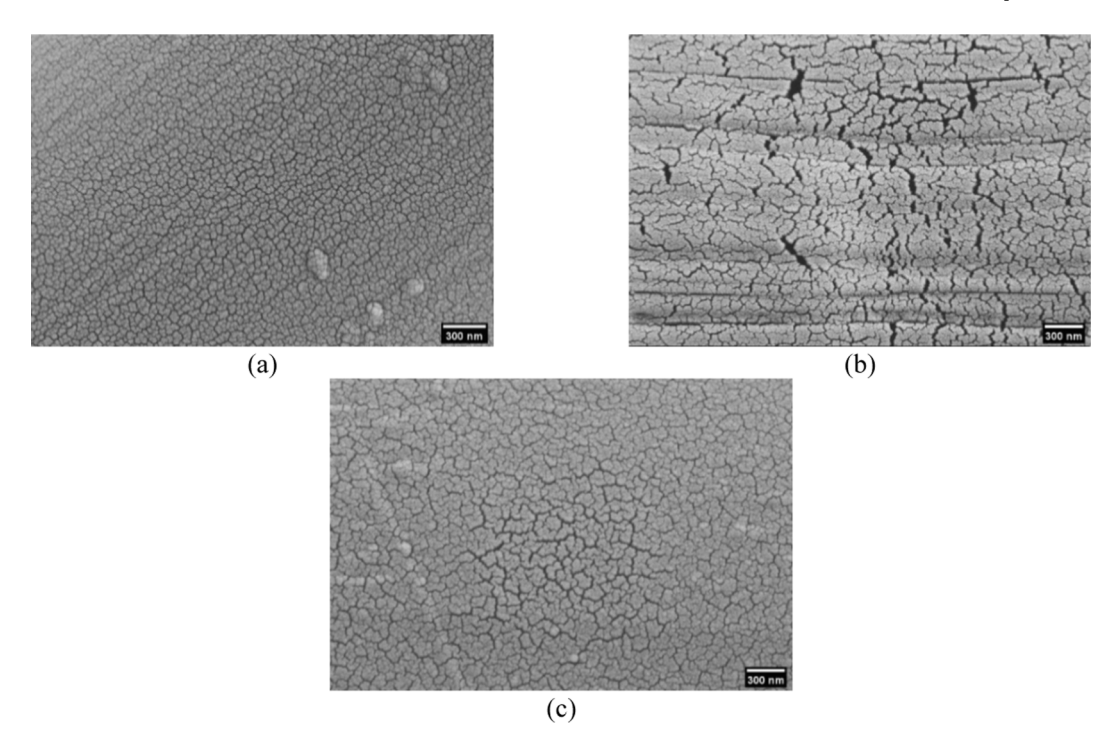


Fig. 16. Speckle pattern on a) unsized IM7 carbon fiber, b) Dyneema® SK76, and c) Kevlar® KM2 fiber using the best sputter coating condition.

$$s_p = \sqrt{\frac{(n_1 - 1)s_1^2 + (n_2 - 1)s_2^2}{n_1 + n_2 - 2}}$$

where, μ_1 and μ_2 , and s_1 and s_2 are sample means and standard deviation for first second sample respectively, n_1 and n_2 are sample size of first and second sample, and s_p is pooled standard deviation.

Degrees of freedom =
$$n_1 + n_2 - 2$$
 (6)

SEM images of failure surfaces for both uncoated and coated specimens are also compared in Fig. 15. The tensile failure surfaces obtained for both uncoated and coated specimens are similar and compare well with a rough, granulated textured failure surface observed for the tensile failure of PAN-based carbon fibers in literature [3,12,52]. To retain failed fiber ends after tensile testing for SEM imaging, additional experiments are performed for both uncoated and coated IM7 single fibers by applying some glycerin onto the fibers before testing. Glycerin is known to help dampen the large energy release at failure that causes multiple failure of the broken fiber end [53,54]. T-test results and similar failure surfaces obtained for uncoated and coated specimens both suggest that the coating has negligible effect on fiber strength. Additionally, the coating is composed of a network of disconnected nanoclusters and has an average thickness (~221 nm) that is only 1/25 of the fiber diameter (~5.2 µm) and therefore is thought to carry negligible loads compared to the fiber. However, in-situ strain measurement of coated fibers and comparison of compliance corrected strains of uncoated and coated fibers is required to gain better insight into the failure of coated fibers.

3.4. Applicability of patterning technique to other fibers

The best patterning condition from sputter coating is also used to investigate pattern creation on other single fibers such as unsized IM7 carbon, Kevlar®, and Dyneema® fibers. This is done in view of investigating the applicability of the patterning technique and the transverse loading experiments to accommodate several types of fibers. Fig. 16 shows the patterns created on unsized IM7 carbon fiber, Kevlar® KM2 (diameter: $12 \mu m$), and Dyneema® SK76 (diameter $17 \mu m$) fibers when

coated using the best sputter coating condition (SC4). The pattern created on unsized IM7 carbon fibers seems to be remarkably like that obtained for the sized IM7 fiber in Fig. 4(d), hence suggesting that we can investigate both sized and unsized IM7 carbon fibers for in-situ transverse loading using the same patterning condition. Patterns obtained on Kevlar® and Dyneema® fibers also show nanoclusters of Au-Pd particles on the fiber surface, although the clusters appear larger in size compared to the patterns obtained on carbon fibers (Fig. 4(d) and 16 (a)) with fewer well-defined boundaries surrounding those clusters. This suggests that the pattern deposited using sputter coating for a given target and sputter coating conditions depends on the substrate material under consideration. This is probably because thin film growth via physical vapor deposition technique such as sputtering mainly occurs via adsorption, diffusion, coalescence, desorption of the target atoms arriving at the substrate surface. The adsorption and diffusion of given target material can vary from substrate to substrate and also with the flux of target atoms arriving at substrate surface [55]. Thus, depending on the target substrate combination some optimization of sputtering conditions such as working pressure, current, coating duration is required to achieve good patterns on the substrate surface for SEM-DIC experiments. However, knowledge regarding the effect of sputtering conditions on pattern formation (see Section 3) can guide the selection of process conditions.

4. Conclusions

In this study, sub-microscale speckle pattern creation on sized IM7 carbon single fibers is shown successfully using sputter deposition. Various process conditions such as working pressure, current, and coating duration are investigated for sputter coating using Au-Pd target to study pattern creation on single carbon fibers. It is found that at longer durations (10 mins) and higher sputtering currents (50 mA), a nanocluster type pattern is obtained on the fiber surface compared to interconnected clusters of nanoparticles at shorter durations (5 mins) and lower current (40 mA). The average nanocluster diameter is approximately 53-54 nm for patterns obtained at a working pressure of 120–140 mTorr (pattern SC4) and 200 mTorr (pattern SC5). To investigate the influence of pattern noise of different patterns, numerical

translation experiments are conducted. Pattern SC4 shows the smallest mean displacement error for a subset size of 61x61 pixel². Decreasing the subset size to 31x31 pixel² results in a two-fold increase in standard deviation in displacement but causes negligible change in the mean displacement error. This is likely an effect of poor subset matching caused by low pattern contrast, thereby requiring larger subsets for better correlation. SEM drift-distortion analysis using 2D-DIC for the pattern SC4 showed significantly higher than expected strain errors associated with rigid body motion caused by the projection of curved (3D) surface on a 2D image plane. Hence, 3D or Stereo-SEM-DIC is needed for accurate measurement of deformation on curved fiber surface. The effect of coating on fiber diameter and fiber tensile strength is investigated for the best sputter coating condition, SC4. Patterning using SC4 condition led to an average increase in fiber diameter of approximately ~221 nm. However, tensile testing results of coated and uncoated fibers suggest there is no significant difference in the mean tensile strength and failure strain between uncoated and coated fibers at 5% significance level. This indicates that patterning the fiber has no significant effect on the fiber strength as required for the in-situ SEM-DIC experiments. Finally, using the best sputter coating condition (SC4), it is shown that this method can be used to create sub-microscale pattern on other single fibers such as unsized IM7 carbon, Kevlar®, and Dyneema® fibers. Although a nanocluster type pattern is also obtained on Kevlar® and Dyneema® fibers, the sputtering conditions may require some tuning to obtain better pattern contrast and smaller nanoclusters.

CRediT authorship contribution statement

Karan Shah: Formal analysis, Investigation, Methodology, Validation, Visualization, Writing – original draft. Subramani Sockalingam: Conceptualization, Methodology, Supervision, Writing – review & editing, Project administration, Funding acquisition. Hannah O'Brien: Data curation, Validation. Gene Yang: Data curation. Mohammad EL Loubani: Data curation. Dongkyu Lee: Conceptualization, Supervision, Project administration, Funding acquisition. Michael A. Sutton: Methodology, Writing – review & editing.

Declaration of Competing Interest

The authors declare that they have no known competing financial interests or personal relationships that could have appeared to influence the work reported in this paper.

Data availability

Data will be made available on request.

Acknowledgements

This material is based upon work supported by the National Science Foundation, CMMI, United States, under Grant No. CMMI – 1915948. Any opinions, findings, and conclusions or recommendations expressed in this material are those of the author(s) and do not necessarily reflect the views of the National Science Foundation. Sized and unsized IM7 carbon fibers used in this study provided by Hexcel corporation is gratefully acknowledged. Dyneema® SK76 fibers used in this work was provided by DSM Dyneema® and is gratefully acknowledged. The authors KS and SS gratefully acknowledge Dr. Hubert Schreier of the Correlated Solutions Inc. for helpful discussions.

References

- [1] Swolfs Y, Morton H, Scott AE, Gorbatikh L, Reed PAS, Sinclair I, et al. Synchrotron radiation computed tomography for experimental validation of a tensile strength model for unidirectional fibre-reinforced composites. Compos Part A Appl Sci Manuf 2015;77:106–13.
- $\hbox{\hbox{$[2]$ Rosen BW. Tensile failure of fibrous composites. AIAA J $1964;2(11):1985-91.}$

- [3] Naito K, Yang JM, Tanaka Y, Kagawa Y. The effect of gauge length on tensile strength and Weibull modulus of polyacrylonitrile (PAN)- and pitch-based carbon fibers. J Mater Sci 2012;47:632–42. https://doi.org/10.1007/s10853-011-5832-x.
- [4] Watanabe J, Tanaka F, Okuda H, Okabe T. Tensile strength distribution of carbon fibers at short gauge lengths. Adv Compos Mater 2014;23:535–50. https://doi.org/ 10.1080/09243046.2014.915120.
- [5] Pickering KL, Murray TL. Weak link scaling analysis of high-strength carbon fibre. Compos Part A Appl Sci Manuf 1999;30:1017–21. https://doi.org/10.1016/S1359-835X(99)00003-2.
- [6] Breite C, Melnikov A, Turon A, de Morais AB, Le Bourlot C, Maire E, et al. Detailed experimental validation and benchmarking of six models for longitudinal tensile failure of unidirectional composites. Compos Struct 2022;279:114828.
- [7] Phoenix SL, Sexsmith RG. Clamp Effects in Fiber Testing. J Compos Mater 1972;6: 322–37. https://doi.org/10.1177/002199837200600311.
- [8] Andersons J, Joffe R, Hojo M, Ochiai S. Glass fibre strength distribution determined by common experimental methods. Compos Sci Technol 2002;62:131–45. https:// doi.org/10.1016/S0266-3538(01)00182-8.
- [9] Scott AE, Mavrogordato M, Wright P, Sinclair I, Spearing SM. In situ fibre fracture measurement in carbon-epoxy laminates using high resolution computed tomography. Compos Sci Technol 2011;71:1471–7. https://doi.org/10.1016/j. compscitech.2011.06.004.
- [10] Shioya M, Inoue H, Sugimoto Y. Reduction in tensile strength of polyacrylonitrile-based carbon fibers in liquids and its application to defect analysis. Carbon N Y 2013;65:63–70. https://doi.org/10.1016/j.carbon.2013.07.102.
- [11] Sugimoto Y, Shioya M, Kageyama K. Determination of intrinsic strength of carbon fibers. Carbon N Y 2016;100:208–13. https://doi.org/10.1016/j. carbon.2016.01.021.
- [12] Okuda H, Young RJ, Tanaka F, Watanabe J, Okabe T. Tensile failure phenomena in carbon fibres. Carbon N Y 2016;107:474–81. https://doi.org/10.1016/j. carbon.2016.06.037.
- [13] Lyons JS, Liu J, Sutton MA. High-temperature deformation measurements using digital-image correlation. Exp Mech 1996;36:64–70. https://doi.org/10.1007/ BE02328699
- [14] Sutton MA, Li N, Garcia D, Cornille N, Orteu JJ, McNeill SR, et al. Metrology in a scanning electron microscope: Theoretical developments and experimental validation. Meas Sci Technol 2006;17(10):2613–22.
- [15] Sutton MA, Li N, Joy DC, Reynolds AP, Li X. Scanning electron microscopy for quantitative small and large deformation measurements Part I: SEM imaging at magnifications from 200 to 10,000. Exp Mech 2007;47:775–87. https://doi.org/ 10.1007/s11340-007-9042-z.
- [16] Sutton MA, Li N, Garcia D, Cornille N, Orteu JJ, McNeill SR, et al. Scanning electron microscopy for quantitative small and large deformation measurements Part II: Experimental validation for magnifications from 200 to 10,000. Exp Mech 2007;47(6):789–804.
- [17] Zhu T, Sutton MA, Li N, Orteu J-J, Cornille N, Li X, et al. Quantitative Stereovision in a Scanning Electron Microscope. Exp Mech 2011;51(1):97–109.
- [18] Kammers AD, Daly S. Digital Image Correlation under Scanning Electron Microscopy: Methodology and Validation. Exp Mech 2013;53:1743–61. https://doi.org/10.1007/s11340-013-9782-x.
- [19] Koohbor B, Montgomery CB, White SR, Sottos NR. Meso-scale strain measurements in fiber reinforced composites. 33rd Tech Conf Am Soc Compos 2018;2018(3): 1542–8. https://doi.org/10.12783/asc33/26028.
- [20] Hudspeth M, Li D, Spatola J, Chen W, Zheng J. The effects of off-axis transverse deflection loading on the failure strain of various high-performance fibers. Text Res J 2015;86:897–910. https://doi.org/10.1177/0040517515588262.
- [21] Sockalingam S, Gillespie JW, Keefe M. Influence of multiaxial loading on the failure of Kevlar KM2 single fiber. Text Res J 2018;88(5):483–98.
- [22] Sockalingam S, Thomas FD, Casem D, Gillespie JW, Weerasooriya T. Failure of Dyneema® SK76 single fiber under multiaxial transverse loading. Text Res J 2019; 89(13):2659_73
- [23] Schreier H, Orteu JJ, Sutton MA. Image correlation for shape, motion and deformation measurements. Basic Concepts, Theory Applications 2009. https:// doi.org/10.1007/978-0-387-78747-3.
- [24] Kammers AD, Daly S. Small-scale patterning methods for digital image correlation under scanning electron microscopy. Meas Sci Technol 2011;22(12):125501.
- [25] Shafqat S, Hoefnagels JPM. Cool, Dry, Nano-scale DIC Patterning of Delicate, Heterogeneous, Non-planar Specimens by Micro-mist Nebulization. Exp Mech 2021;61:917–37. https://doi.org/10.1007/s11340-020-00686-2.
- [26] Scrivens WA, Luo Y, Sutton MA, Collette SA, Myrick ML, Miney P, et al. Development of patterns for digital image correlation measurements at reduced length scales. Exp Mech 2007;47(1):63–77.
- [27] Montgomery CB, Koohbor B, Sottos NR. A Robust Patterning Technique for Electron Microscopy-Based Digital Image Correlation at Sub-Micron Resolutions. Exp Mech 2019;59:1063–73. https://doi.org/10.1007/s11340-019-00487-2.
- [28] Kammers AD, Daly S. Self-Assembled Nanoparticle Surface Patterning for Improved DIC in a SEM. Exp Mech 2013;53:1333–41.
- [29] Berfield TA, Patel JK, Shimmin RG, Braun PV, Lambros J, Sottos NR. Micro-and nanoscale deformation measurement of surface and internal planes via digital image correlation. Exp Mech 2007;47:51–62. https://doi.org/10.1007/s11340-006-0531-2.
- [30] Pal R, Sung KE, Burns MA. Microstencils for the patterning of nontraditional materials. Langmuir 2006;22:5392–7. https://doi.org/10.1021/la052811s.
- [31] Collette SA, Sutton MA, Miney P, Reynolds AP, Li X, Colavita PE, et al. Development of patterns for nanoscale strain measurements: I. Fabrication of imprinted Au webs for polymeric materials. Nanotechnology 2004;15(12):1812–7.

- [32] Sabaté N, Vogel D, Keller J, Gollhardt A, Marcos J, Gràcia I, et al. FIB-based technique for stress characterization on thin films for reliability purposes. Microelectron Eng 2007;84(5-8):1783-7.
- [33] Zhu R, Xie H, Xue Y, Wang L, Li YanJie. Fabrication of speckle patterns by focused ion beam deposition and its application to micro-scale residual stress measurement. Meas Sci Technol 2015;26(9):095601.
- [34] Guo SM, Sutton MA, Li N, Li XD, Wang LW, Rajan S. Measurement of Local Thermal Deformations in Heterogeneous Microstructures via SEM Imaging with Digital Image Correlation. Exp Mech 2017;57:41–56. https://doi.org/10.1007/ s11340-016-0206-6.
- [35] Dong YL, Pan B. A Review of Speckle Pattern Fabrication and Assessment for Digital Image Correlation. Exp Mech 2017;57:1161–81. https://doi.org/10.1007/ s11340-017-0283-1
- [36] Hoefnagels JPM, van Maris MPFHL, Vermeij T. One-step deposition of nano-to-micron-scalable, high-quality digital image correlation patterns for high-strain insitu multi-microscopy testing. Strain 2019;55:1–13. https://doi.org/10.1111/csr.12320
- [37] Fiber C. HexTow ® IM7 2020:1–2. https://www.hexcel.com/user_area/content_media/raw/IM7_HexTow_DataSheet.pdf.
- [38] Safi I. Recent aspects concerning DC reactive magnetron sputtering of thin films: a review. Surf Coatings Technol 2000;127(2-3):203–18.
- [39] Bobzin K, Bagcivan N, Immich P, Bolz S, Alami J, Cremer R. Advantages of nanocomposite coatings deposited by high power pulse magnetron sputtering technology. J Mater Process Technol 2009;209:165–70. https://doi.org/10.1016/j. imaturotec. 2008.01.035
- [40] Jung YS, Lee DW, Jeon DY. Influence of dc magnetron sputtering parameters on surface morphology of indium tin oxide thin films. Appl Surf Sci 2004;221:136–42. https://doi.org/10.1016/S0169-4332(03)00862-6.
- [41] Montgomery CB. Multiscale Characterization of Carbon Fiber-Reinforced Epoxy Composites. University of Illinois at Urbana-Champaign, 2018.
- [42] Tanaka Y, Naito K, Kishimoto S, Kagawa Y. Development of a pattern to measure multiscale deformation and strain distribution via in situ FE-SEM observations. Nanotechnology 2011;22(11):115704.

- [43] Otsu N, Smith PL, Reid DB, Environment C, Palo L, Alto P, et al. Otsu_1979_otsu_method. IEEE Trans Syst Man Cybern 1979;C:62–6.
- [44] Pan B, Xie H, Wang Z, Qian K, Wang Z. Study on subset size selection in digital image correlation for speckle patterns. Opt Express 2008;16:7037. https://doi.org/ 10.1364/oe.16.007037.
- [45] Pan B, Lu Z, Xie H. Mean intensity gradient: An effective global parameter for quality assessment of the speckle patterns used in digital image correlation. Opt Lasers Eng 2010;48:469–77. https://doi.org/10.1016/j.optlaseng.2009.08.010.
- [46] Reu PL, Toussaint E, Jones E, Bruck HA, Iadicola M, Balcaen R, et al. DIC Challenge: Developing Images and Guidelines for Evaluating Accuracy and Resolution of 2D Analyses. vol. 58. 2018. https://doi.org/10.1007/s11340-017-0349-0.
- [47] Schreier HW, Sutton MA. Systematic errors in digital image correlation due to undermatched subset shape functions. Exp Mech 2002;42:303–10. https://doi.org/ 10.1177/001448502321548391.
- [48] Reu PL. Experimental and Numerical Methods for Exact Subpixel Shifting. Exp Mech 2011;51:443–52. https://doi.org/10.1007/s11340-010-9417-4.
- [49] Schreier HW, Braasch JR, Sutton M a. On systematic errors in digital image correlation. Opt Eng 2000;39:2915–21.
- [50] ASTM C1557-03. Standard Test Method for Tensile Strength and Young's Modulus of Fibers. American Society for Testing and Materials 2014;03:1–10. https://doi. org/10.1520/C1557-03R13.2.
- [51] Lyons KM, Newcomb BA, McDonald KJ, Chae HG, Kumar S. Development of single filament testing procedure for polyacrylonitrile precursor and polyacrylonitrilebased carbon fibers. J Compos Mater 2015;49:2231–40. https://doi.org/10.1177/ 0021998314545184
- [52] Chae HG, Newcomb BA, Gulgunje PV, Liu Y, Gupta KK, Kamath MG, et al. High strength and high modulus carbon fibers. Carbon N Y 2015;93:81–7.
- [53] Bennett SC. Strength/structure relationships in carbon fibres. J Mater Sci 1983;18: 3337–47. https://doi.org/10.1007/BF00544159.
- [54] Da Silva JLG, Johnson DJ. Flexural studies of carbon fibres. J Mater Sci 1984;19: 3201–10. https://doi.org/10.1007/BF00549805.
- [55] Rockett A. The Material Science of Semiconductors. Mater. Sci. Semicond., New York: Springer Science+Business Media; 2008, p. 455–502.